Optimizing silver-capped silicon nanopillars to simultaneously realize macroscopic, practical-level SERS signal reproducibility and high enhancement at low costs

Wu, Kaiyu; Rindzevicius, Tomas; Schmidt, Michael Stenbæk; Thilsted, Anil Haraksingh; Boisen, Anja

Published in:
Journal of Raman Spectroscopy

Link to article, DOI:
10.1002/jrs.5255

Publication date:
2017

Document Version
Peer reviewed version

Optimizing Silver-capped Silicon Nanopillars to Simultaneously Realize Macroscopic, Practical-level SERS Signal Reproducibility and High Enhancement at Low Costs

Kaiyu Wu[a,b]*, Tomas Rindzevicius[a,b], Michael S. Schmidt[a,b], Anil H. Thilsted[a] and Anja Boisen[a,b]

a Technical University of Denmark, Department of Micro- and Nanotechnology, Ørsteds Plads, Building 345B, 2800 Kgs. Lyngby, Denmark

b DNRF and Villum Fonden Center for Intelligent Drug Delivery and Sensing Using Microcontainers and Nanomechanics, IDUN, Ørsteds Plads, Building 345C, 2800 Kgs. Lyngby, Denmark

Surface-enhanced Raman spectroscopy, Nanopillars, SERS uniformity, SERS reproducibility, Maskless reactive ion etching

ABSTRACT: The ideal surface-enhanced Raman spectroscopy (SERS) substrate should fulfil the following: i) predictable SERS enhancement, ii) macroscale SERS signal uniformity, and iii) suitability for mass production at low costs. Macroscale SERS uniformity and reproducibility at practical levels are big obstacles which have been preventing most SERS substrates from reliable sensing applications. We have previously shown that SERS-active nanopillar structures, fabricated by lithography-free processes, exhibit high average SERS enhancements and are mass producible. Here, we report an optimized process and show that the improved structures exhibit unrivalled macroscale SERS uniformities (RSD: ~2.5% in mm scale, ~7% in wafer scale) and reproducibility (RSD: ~1.5% across three wafers), while at the same time exhibiting a very large average SERS enhancement factor of > 10^8. The obtained SERS uniformity (~2.5% RSD in mm scale) is the best to date measured on large-area solid SERS substrates. Fast and reproducible SERS analysis of trans-1,2-bis (4-pyridyl) ethylene down to 4 x 10^{-13} mol is demonstrated using the optimized structures. We emphasize that achieving simultaneously macroscopic, practical-level SERS signal reproducibility and high enhancement via a lithography-free process is a notable advance towards industrialization of substrate-based SERS sensors.

INTRODUCTION

Surface-enhanced Raman spectroscopy (SERS) is a powerful analytical technique for a vast range of chemical and biological sensing applications.[1-4] It is an ultrasensitive and label-free detection method.

With the aid of the significantly enhanced localized electrical fields near the surfaces of noble metallic nanostructures, called “hot spots”,[5] SERS can reveal the vibrational modes of target molecules located inside those hot spots.[6,7] To sense a single molecule, a SERS enhancement factor (EF) above 10^9 should be achieved.[8]

SERS-active materials can be divided into two categories: nanoparticle colloidal suspensions and structural solid substrates. For both, it would be ideal if the plasmonic nanostructures are chemically stable, easy to prepare in a reproducible manner, and exhibit a spatially uniform, high EF.[9] To achieve reproducible and quantitative SERS analyses, one way is to fabricate SERS-active materials in a repeatable way and to improve the uniformity of the hot spots.

A number of SERS-active metallic nanoparticles in colloidal solutions have been synthesized, including shell-isolated nanoparticles,[10] core-shell nanoparticles,[11] and nanoparticles with sharp features.[12,13] The main advantage of them is their high EFs caused by (i) intra- or inter particle plasmonic couplings, and (ii) lightning-rod effect that is specifically pronounced in metallic nanoparticles with sharp features. Since EF is extremely sensitive to the inter particle spacing, it is necessary to control the size of the gap junctions between nanoparticles to achieve a spatially uniform EF. For example, bio-template assisted synthesis can be used to realize sub-10 nm distance control between nanoparticles.[14] Recently, reliable and quantitative SERS analysis has been achieved using core–shell nanoparticles with embedded internal standards,[15] or alkanethiolate ligand-regulated silver nanoparticle films.[16]

A vast variety of top-down process flows have been employed to fabricate large-area, SERS-active structural solid substrates.[17] Most of them are lithography-based techniques, which first tailor mask layers to form different nanostructured patterns, that are then transferred into a variety of substrate materials. The realized structures are subsequently metalized to make the surface SERS-active.[18-22] Strong EFs are obtained at hot spots formed either at the gap junctions between individual structures, [23-25] or at the metallic nanogrooves [26] and nanotips.[27,28] Structural solid SERS substrates usually exhibit more reproducible SERS signals across larger surface areas compared to colloidal nanoparticle systems, at the cost of lower EFs.[29-31]

Examples of structural solid SERS substrates include SERS-active structures fabricated on rose petals. They exhibit EFs of above 10^8 and good uniformity across randomly chosen locations.[32] Another example is the immobilized nanorod assembly substrates whose fabrication process is large-format and repeatable. They exhibit reproducibly high EFs with good signal uniformity.[33,34] Overall, at

a practical level, there are few substrates that simultaneously demonstrate suitability for mass production, and reproducibly high EFs over macroscale areas or across different samples.

Using a lithography-free reactive ion etch (RIE) process followed by e-beam assisted metal evaporation, we have developed wafer-scale silver capped silicon nanopillars (NPs) with a high aspect ratio and used these as SERS substrates.[35-37] A principle scheme of their fabrication process is shown in scheme 1. The fabricated NPs are flexible and will lean towards their nearest neighbors as deposited analyte solution evaporates, creating self-assembled SERS hot spots in which the analyte molecules are located. Average EFs of above 10^8 and detection limit down to 10^{-10} M have been achieved.[37] Applications such as detecting nerve gases has been realized on such substrates with report high sensitivities.[38] A key advantage of such SERS substrates is their simple fabrication process. The fabrication procedure is fast, repeatable and does not require any lithographic steps. The very low fabrication costs enable these SERS substrates to be used as cheap and single-use consumables.

In spite of the aforementioned advantages, challenges remain for the NP substrate to facilitate reproducible SERS signals. According to our previous report,[37] the SERS intensities of the NP substrate exhibit a relative standard deviation (RSD) of around 14% across a 5 × 5 mm^2 surface area. We have yet to demonstrate a good macroscale reproducibility of the SERS signal at a practical level.

Macroscale SERS uniformity is a fundamental prerequisite to achieve reliable measurements, and is a prerequisite if quantitative SERS is to be realized. The aim of this work is to tackle macroscale EF uniformity issues for the NP substrate by means of an improved nanofabrication process. In SERS, the overall signal can be considered the sum of the signals contributed by all analytes located in the hot spots probed by the excitation laser. Inhomogeneity of the SERS signals can be ascribed to (i) the electrical field enhancement in the hot spots being sensitive to the detailed shape of plasmonic nanostructure as well as the coupling between nanostructures, that can vary by several orders of magnitude,[39] and (ii) the uneven distribution of analytes in individual hot spots.

To improve SERS uniformity and reproducibility for the NP substrate, one approach is to increase the density of the NPs. In this case, the leaning NPs are expected to form larger and denser packed clusters that exhibit more uniform distribution of hotspots over the substrate surface area. There is a need for further experimental work to (i) find and systematically evaluate the experimental parameters that affect the density of the NPs, and subsequently (ii) modify and optimize the lithography-free process to fabricate high-density NPs that exhibit macroscale SERS uniformities and reproducibility, and meanwhile a

large SERS enhancement factor, that would consequently qualify them for reliable and high-performance SERS analyses.

In this paper, we first provide insights into the mask-less RIE process that produces Si NPs on a 4-inch Si wafer. We show that by decreasing the chamber pressure during etching, the density of the fabricated NPs can be systematically increased. Thereby, NPs of uniform heights with a significantly increased density as high as approximately 48 NPs μm^{-2} can be fabricated. These structures are able to form, via leaning, large and densely packed clusters that exhibit much more uniformly spaced hot spots, compared to the NP arrays with lower densities, as shown by fig. 1. In addition, systematic optimization on etching time and metal thickness are performed for the high-density NP substrates to achieve an optimal SERS EF. Next, macroscale SERS uniformity and wafer-to-wafer SERS reproducibility are evaluated for the optimized structures. SERS RSDs of around 2.5% are observed across 1 mm distances. Inch-scale SERS RSDs of around 6% are achievable, and averaged SERS intensities exhibit an RSD of around 1.5% across three wafers. This indicates that the optimized process is capable of fabricating NPs of super-high density with macroscale SERS uniformity, and more importantly, with excellent reproducibility. Lastly, an example of SERS analyses using the optimized structures is given. Using two sets of specimens of $\sim 1 \times 1$ cm^2 surface areas taken from two wafers, fast and reproducible SERS analyses of trans-1,2-bis (4-pyridyl) ethylene (BPE) from 4×10^{-13} mol to 10^{-8} mol are demonstrated. Our experimental findings demonstrate that the improved super-high density NPs, fabricated by the optimized lithography-free process, are strong candidates for obtaining very reproducible and reliable SERS spectra at low costs.

EXPERIMENTAL METHODS

Fabrication of SERS nanopillars: The fabrication process can be divided into three parts. First, starting from a 4-inch Si wafer, a mask-less RIE was employed to form Si NPs with radii $\approx 20 \pm 4$ nm. P-type single-side (100) polished wafers were used (Topsil). Mask-less RIE was performed in an Advanced Silicon Etcher (Surface Technology Systems MESC Multiplex ICP) at an SF_6:O_2 flow ratio of 1.12, a platen power of 120 W, and a chamber pressure from 18 mTorr to 36 mTorr depending on the required NP density. The employed etching time was 255 seconds. Si NPs were formed at a rate of $\sim$3 nm/s. Next, an O_2 plasma treatment was applied to remove RIE by-products from the surface of the Si NPs. An O_2 flow of 45 sccm, a platen power of 20 W, a coil power of 800 W, and a chamber pressure of 10 mTorr were used. The time of the O_2 plasma treatment was 1 minute. Lastly, a 185 nm thick Ag film was deposited onto the Si NPs by e-beam evaporation. An Alcatel SCM 600 was used for the deposition at a pressure of $\sim 2 \times 10^{-6}$ mbar, with a deposition rate of 10 Å/s. The deposition resulted in

the formation of Ag caps at the apex of the Si NPs, along with an Ag film on the underlying Si surface. Representative cross-sectional SEM images of the fabricated Si NPs are shown in fig. 1. Silver was chosen due to its favorable dielectric function which results in strong plasmonic resonances for the NPs with the applied Raman laser excitation at a 780 nm wavelength.[40] The manufactured substrates are stored in a vacuum Thermo Scientific Nalgene desiccator to minimize oxidation.

SEM characterization: SEM images were recorded using a Zeiss Supra 40VP field emission scanning electron microscope with a maximum spatial resolution of 1.0 nm. An in-lens detector was used. A working distance of ~2 mm and an acceleration voltage of 8.0 kV were used. The angle between the incident electron beam and the surface of the Si NPs was 90° and 0° for top-view and cross-sectional imaging, respectively.

SERS measurements: A Thermo Scientific DXR confocal Raman microscope with a spatial resolution of 1 μm and a confocal depth of 2 μm was used for all the SERS measurements. The microscope was coupled to a single grating spectrometer with a 5 cm^{-1} FWHM spectral resolution and a ± 2 wavenumber accuracy. All Raman measurements were conducted at room temperatures. The absolute Raman intensities of the instrument over its detectable spectral range were calibrated according to a known lamp spectrum along with the Raman signal produced on solid polystyrene. For SERS measurements on the NPs, unless otherwise noted, a 25 μm slit and a 10X objective lens were used; an excitation wavelength of 780 nm was employed with a laser spot of ~3.1 μm in diameter; a step size of 10 μm (100 μm for fig. 5) was used. A 1 μL volume of BPE dissolved in ethanol was deposited onto a NP specimen. The deposited droplet spread over the whole specimen area of ~1 × 1 cm^2 and completely evaporated in a few seconds. The fabricated NPs were flexible and leaned towards their nearest neighbours as the deposited analyte solution evaporated, creating self-assembled SERS hot spots in-between and at the necks of the Ag caps.[40] Top-view SEM images of the leaning NPs of two different densities (~19 NPs μm^{-2} and ~48 NPs μm^{-2}) can be found in fig. 1a.

Dark-field scattering measurements: A Nikon Ti-U inverted microscope was used with a CF LU Plan Fluor Epi 50X objective, which had a working distance of 1 mm and a NA of 0.8. The incident angle was ~50°. The scattered light was collected from the center of the objective and was subsequently guided into a spectrometer (Shamrock Spectrograph SR-303I-A, equipped with Andor Newton 970 EMCCD).

RESULTS AND DISCUSSIONS

Density control in the lithography-free process: To overcome the issue of macroscale SERS signal uniformity and reproducibility for the NP substrate, our approach is to first fabricate NPs of a significantly increased density. In this section, we demonstrate how the density of NPs can be controlled and predicted in the employed lithography-free process.

It was found, that during the RIE, the pressure of the chamber has an influence on the density of the fabricated Si NPs. To gain a better control of the process, it was logical to perform a systematic study to reveal the relationship between p, the RIE chamber pressure, and D, the density of NPs. This was specifically done by (i) fabricating NPs under four different values of p, ranging from 18 mTorr to 36 mTorr, followed by (ii) SEM characterization of these NPs both before and after clustering. The results are shown in fig. 2.

It can be seen from fig. 2b-d that a lower p leads to a higher D. Lowering the chamber pressure increases the mean free path of the reactive ions, and thus intensifies the anisotropic etch. Initially formed Si pillars are vulnerable to isotropic etch, thus a more anisotropic RIE retains more pillars, and increases the density of NPs. To quantify such an effect, D versus p is plotted using double logarithmic axes, shown in fig. 2a. It can be seen that by decreasing p from 36 mTorr to 18 mTorr, D increases from ~19 NPs μm^{-2} to ~48 NPs μm^{-2}. Furthermore, fig. 2a shows that D exhibits a monomial dependence on p, as is indicated by the linear fit in the log-log plot with a correlation of $R^2 = 0.98$. Therefore, the following equation:

$$D = ap^b \tag{1}$$

, where $a = 3000$, $b = -1.433$, and $p \in [18, 36]$ mTorr is established to estimate the density of NPs D, given the value of the RIE chamber pressure p.

Further reducing the RIE chamber pressure leads to the production of irregular NPs with non-uniform heights. Fig. 3b and 3c show the irregular NPs fabricated under p of 16 mTorr and 12 mTorr, respectively. For these structures, at the apex of Si NPs, due to the significant variation in heights, regular Ag caps in the same horizontal plane cannot form. As a result, SERS performance degrades, since densely clustered Ag caps with uniform nanogaps no longer form via leaning of the NPs. In fig. 3a, it is seen that irregular NPs fabricated under p of 16 mTorr and 12 mTorr exhibit ~30% and ~15% of the SERS signal obtained on NPs with a uniform height fabricated under a p of 18 mTorr. Based on the results above, it is reasonable to set p = 18 mTorr as the optimized RIE chamber pressure for obtaining high-density Si NPs, as applying it produces NPs of the highest density (~48 NPs μm^{-2})

with a uniform height. It should be pointed out that in previous reports related to the NPs made by a lithography-free process, [35-38, 40-45] only substrates with NPs of low densities less than ~19 NPs μm^{-2} were used.

For the high-density Si NPs, fixing p = 18 mTorr as the employed RIE chamber pressure, the fabrication process can be further optimized in terms of SERS EF, by changing RIE etching time and Ag deposition thickness. Systematic optimization results are shown in fig. S1 (Supporting Information). It was found that by employing 255 seconds of etching with an Ag deposition thickness of 185 nm, a maximum SERS signal was obtained. The calculated average SERS EF across the optimized substrate is ~1.1 x 10^8. Details of the calculation can be found in the supplementary information.[46,47]

Additionally, dark-field scattering measurements were carried out on the optimized NPs. Results are shown in fig. S2 (Supporting Information). The scattering intensity of the leaning NPs displays a maximum around 800 nm, which is close to the wavelength of the employed Raman laser (780 nm). Near the scattering maximum, the NP structures efficiently support the following localized surface plasmon resonance (LSPR) modes: (i) the cavity mode, which generates electromagnetic hot spots near the bottom of the Ag caps, and (ii) the hybridized mode, which generates electromagnetic hot spots in the gap junctions between adjacent Ag caps. The efficient generation of these hot spots leads to the significant electromagnetic SERS enhancement for the NP substrate. Detailed theoretical and experimental investigations regarding the LSPRs of such type of structures can be found in the reference. [40]

Influence of NP density on SERS uniformity: In this section, the influence of the density of NPs on the SERS uniformity is investigated. Three ~1 x 1 cm^2 NP specimens, fabricated under different RIE chamber pressures were used. The employed pressure was 18 mTorr, 24 mTorr and 36 mTorr, producing substrates with a density of ~48 NPs μm^{-2}, ~31 NPs μm^{-2} and ~19 NPs μm^{-2}, accordingly. The NPs leaned towards their neighbors and clusters of NPs were formed after pipetting and drying of 1 µL 10^{-4} M BPE in ethanol solution. The droplet immediately spread over the whole specimen area and completely evaporated several seconds thereafter. SEM images of the NPs were taken both before and after leaning (fig. 2b-d). SERS line scans were then conducted on all the specimens. Each line scan was 1 mm long with a step size of 10 µm. The obtained spectra are shown in fig. 4b. The SERS intensities at the 1641 cm^{-1} peak were averaged, and the corresponding RSDs were calculated. The results are shown in fig. 4a. It can be seen that the SERS RSD decreases from ~10.5% to ~4.5% when increasing the NP density from ~19 NPs μm^{-2} to ~48 NPs μm^{-2}. Such a result confirms our hypothesis, that an increasing density would improve the SERS uniformity. By increasing NP density, the leaning

NPs form larger and more densely packed clusters that exhibit more uniform distribution of hotspots over the substrate surface area, due to the closer distance between each NP and its neighbours. This effect can be clearly seen in fig. 2b-d from the SEM images of the clustering NPs. Besides, the SERS intensity increases when increasing NP density. As shown by fig. 4a, the averaged SERS intensity of the 1641 cm^{-1} peak increases by ~50% when increasing NP density from ~19 NPs μm^{-2} to ~48 NPs μm^{-2}. This is reasonable, since the laser spot covers a greater number of hot spots for NPs with a higher density, as has been illustrated in fig. 1a.

Large-area SERS uniformity and wafer-to-wafer SERS reproducibility of the densely clustered nanopillars: Here, we investigate and demonstrate even larger scale SERS uniformity and wafer-to-wafer SERS reproducibility for the optimized densely clustered NPs. For such purposes, we performed SERS line scans on three wafers. Each line scan started from the center of the 4-inch wafer and ended at its edge, with a step size of 100 μm. The schematic in fig. 5a shows the track of the line scan. The analyte was 10^{-4} M BPE in ethanol. The incubation time was less than 5 seconds. Fig. 5b shows the line scanned SERS spectra. It can be seen that for all the three wafers, the SERS intensity remains high until half way towards the wafer edge, whereafter it decreases dramatically. To quantify such an effect, fig. 5e plots the trajectory of the SERS intensities at the 1641 cm^{-1} BPE peak for wafer 1. It can be seen that between 0 - 0.75 inch from the center of the wafer, the SERS signal remains relatively stable. It then gradually decreases after the 0.75-inch point, and falls dramatically after the 1-inch point. This is also true for the other two wafers. As shown in fig. 5c and 5d, for all the three wafers, after extending the statistical region from 0 – 0.75 inch to 0 – 1 inch, the averaged SERS signal of the 1641 cm^{-1} BPE peak decreases with an increased RSD. In addition, fig. 5c shows that the high-density Si NPs exhibit an extremely long-range SERS uniformity, which is ~7% across 0.75 inch, with the averaged SERS intensities exhibiting a RSD of ~1.5% across the three wafers, indicating an excellent reproducibility of the fabrication process. Such results imply that in order to carry out reproducible and reliable SERS analysis, one should only use specimens in a circle, which is homocentric with the 4-inch wafer and has a 1.5-inch diameter. To improve yield, the whole process can be transferred to 6-inch or 8-inch wafers or larger, since the drop of the SERS intensity towards the edge of the wafer is hypothesized to be due to the macro loading effect during the mask-less RIE process.[48] The macro loading effect alters and randomizes the morphology of the NPs which are close to the edge of the wafer, as is shown in the SEM images in fig. 5a.

Reproducible SERS analysis on high-density nanopillars: Finally, we show an example of reproducible and reliable SERS analysis of trace-amount trans-1,2-bis (4-pyridyl) ethylene using the

optimized super high-density NP structures. SERS analyses of extremely small sample volumes (1 μL) containing BPE in ethanol from 4 x 10^{-13} mol to 10^{-8} mol were performed on two sets of specimens, taken respectively from two wafers. Each specimen had ~1 x 1 cm^2 surface area. In this study, a very small sample volume (1 μL) was chosen since being able to sense analytes in small sample volumes in a short time is favourable for many practical applications.[49,50] It is worth noting that sensing analyte of low concentrations becomes harder at smaller sample volumes, since the absolute number of the analyte molecules decreases. This consequently reduces the number of analyte molecules that can adhere to the substrate surface, resulting in weaker and more inhomogeneous SERS signals. To compensate the uneven distribution of the analytes on the surface of the NPs at low quantities, a SERS line scan of 1 mm distance with a step size of 10 μm composed one analysis. Doing this essentially increased the total probing area of the Raman laser by 100 times. It is noteworthy that the analysis was still fast, since measuring an individual spot took 3 seconds (1 s exposure x 3 times). For each analysis, we recorded the averaged SERS intensity and the corresponding RSD at the 1641 cm^{-1} BPE Raman peak.

The recorded intensities of the 1641 cm^{-1} BPE Raman peak for all the samples are shown in fig. S3 (Supporting Information). Quantized results are shown in fig. 6a and 6b. It can be seen from fig. 6a that the SERS analysis is highly reproducible and reliable. This indicates that (i) densely clustered NPs exhibit excellent SERS uniformities across macroscale areas (inch-scale) at a practical level, via the significantly improved hot spot density and uniformity, and (ii) the optimized fabrication process is reproducible and is suitable for industrial mass production. Additionally, fig. 6b shows that the RSD increases from ~2.5% to ~25% when the quantity of BPE decreases from 10^{-9} mol to 4 x 10^{-13} mol, due to the enhanced uneven distribution of the analytes on the NPs. To quantitatively sense even less amount of BPE, the analyses should be performed with the aid of additional techniques, such as surface functionalization and analyte condensation, which is out of the scope of this study.

CONCLUSION

Large-area and reproducible fabrication of improved NPs with super-high density are achieved using an optimized lithography-free process. The influence of the chamber pressure during the RIE on the density of the NPs is systematically studied. The optimized NPs (~48 NPs μm^{-2}) exhibit unrivalled macroscale SERS signal uniformity, due to their ability to form extraordinary dense and uniform hot spots. Furthermore, by systematic optimization on etching time and metal thickness, the improved NPs exhibit macroscale SERS uniformities (RSD: ~2.5% in mm scale, ~7% in wafer scale) and reproducibility (RSD: ~1.5% across three wafers), plus a very large average SERS enhancement factor

of $>10^8$, which are rarely achieved simultaneously. The reported SERS uniformity (~2.5% RSD in mm scale) is the best to date measured on a large-area solid SERS substrate. Our experimental findings demonstrate that the optimized super-high density NPs are strong candidates for obtaining reproducible and reliable SERS spectra at a practical level. We emphasize that achieving simultaneously macroscopic, practical-level SERS signal reproducibility and high enhancement via a lithography-free process is a notable advance towards industrialization of substrate-based SERS sensors. From a practical point of view, the presented SERS substrates are particularity interesting since they are easy to handle and store and the fabrication is scalable, facilitating a wide and simple use of SERS in sensing applications.

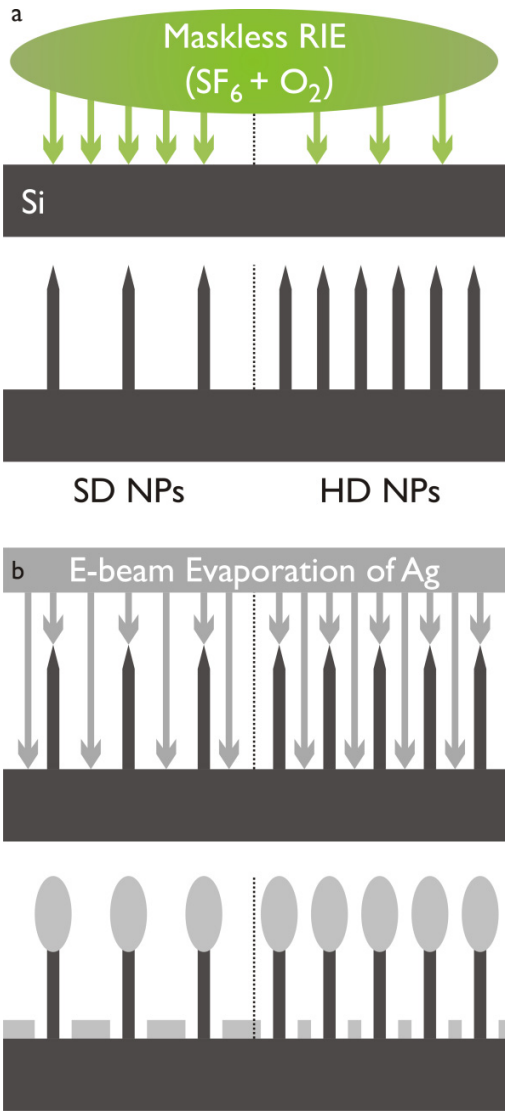

Scheme 1. The lithography-free fabrication of SERS NPs. (a) Mask-less RIE is employed to form Si NPs on a 4-inch Si wafer. SF_6 and O_2 are the gas sources of the reactive ions. A lower chamber pressure leads to a higher NP density. (b) Ag is deposited to the Si NP surface by e-beam evaporation. The deposition leads to the formation of Ag caps at the apex of the Si NPs, along with an Ag film on the underlying Si surface.

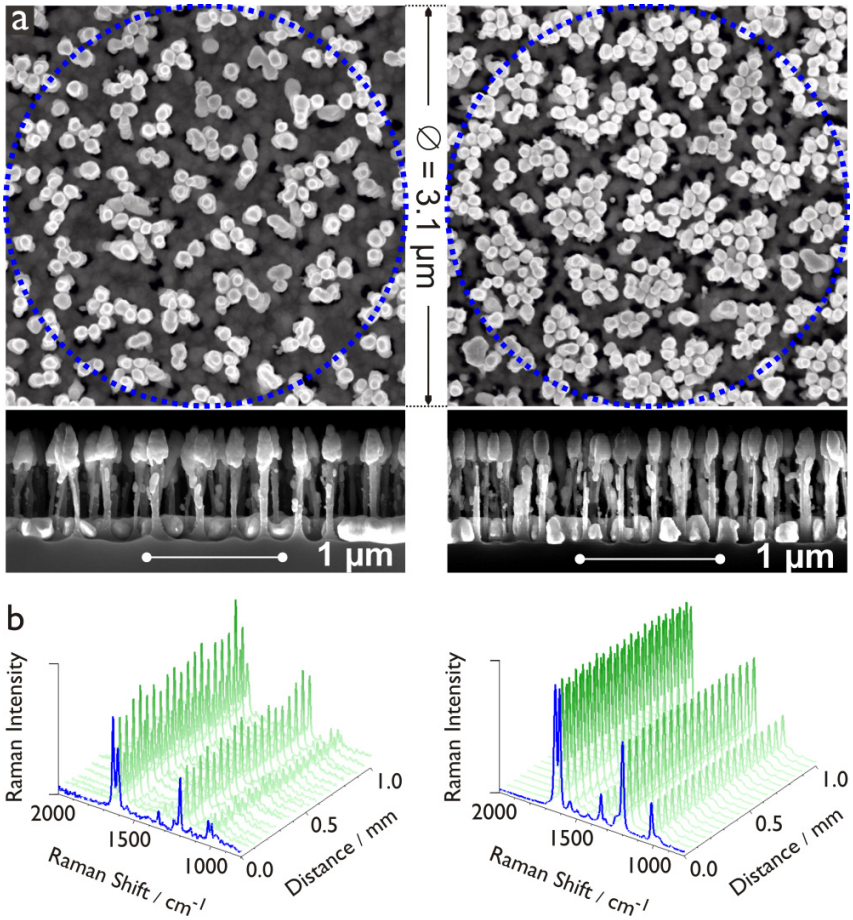

Fig. 1 (a) Top-view and cross-sectional SEM images of the Si NPs before and after optimization. The density of the NPs is ~19 NPs μm^{-2} and ~48 NPs μm^{-2} for the left image (NPs before optimization) and right image (optimized NPs), respectively. On the top-view images, the NPs are leaned by pipetting and drying of 1 µL 10^{-3} M BPE in ethanol solution. The dotted circles represent the spot area of the SERS excitation laser. (b) Two scanned SERS spectra across 1 mm lines, acquired correspondingly on the NP substrate shown in (a) above each. For clarity, one scan shows 20 spectra.

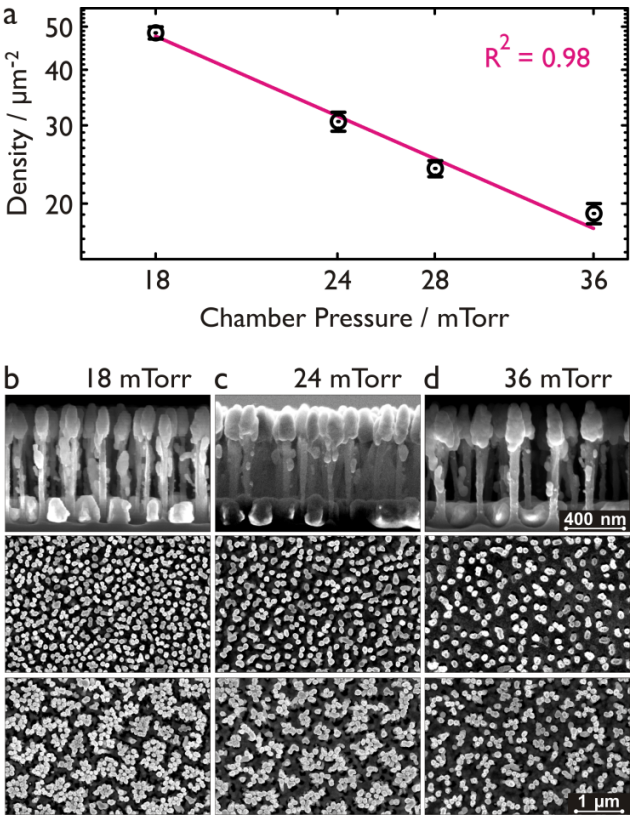

Fig. 2 (a) Log-log plot for the density of the NPs *D* versus the RIE chamber pressure *p*. (b)-(d) Representative SEM images for the NPs fabricated with a RIE chamber pressure of 18 mTorr, 24 mTorr and 36 mTorr, separately. From the first row to the third row, cross-sectional images, top-view images of the vertical NPs, and top-view images of the leaning NPs are shown in sequence. The Ag deposition thickness was 185 nm for all the samples.

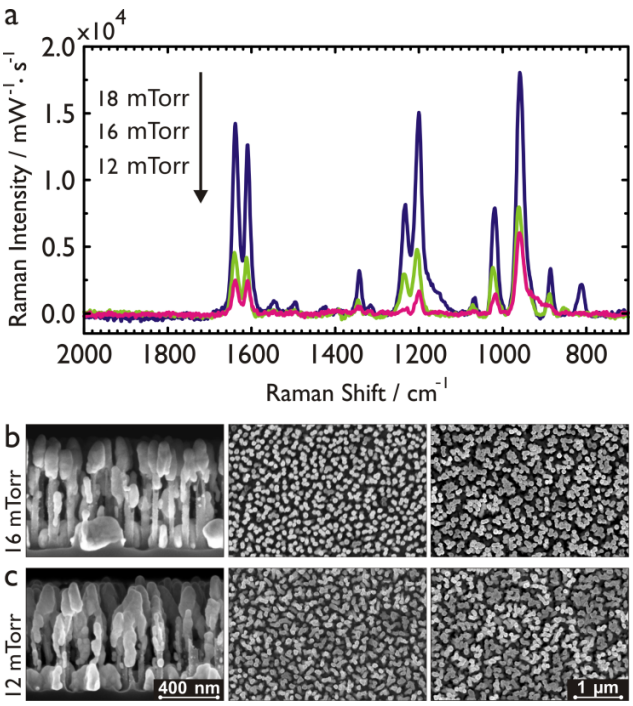

Fig. 3 (a) SERS spectra of BPE measured on NPs fabricated using different RIE chamber pressures. The NPs were leaned by pipetting and drying of 1 μL 10^{-4} M BPE in ethanol solution. (b) and (c) Representative SEM images for the NPs fabricated using a RIE chamber pressure of 16 mTorr and 12 mTorr, respectively. From the first column to the third column, cross-sectional images, top-view images of the vertical NPs, and top-view images of the leaning NPs are shown.

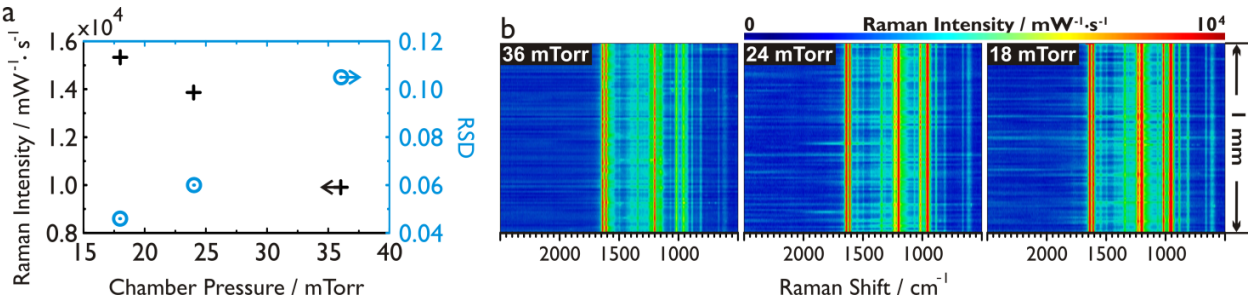

Fig. 4 (a) The averaged SERS intensities and the corresponding RSDs at the 1641 cm^{-1} BPE peak for NPs of different densities fabricated under different RIE pressures, obtained from the scanned spectra in (b). (b) SERS line scans of BPE on three specimens containing NPs fabricated under different RIE chamber pressures. The employed pressure *p* was 18 mTorr, 24 mTorr and 36 mTorr, producing NPs with a *D* of ~48 NPs μm^{-2}, ~31 NPs μm^{-2} and ~19 NPs μm^{-2}, accordingly. The NPs leaned towards their neighbors and clusters of NPs were formed after pipetting and drying of 1 µL 10^{-4} M BPE in ethanol solution. SEM images of the NPs before and after leaning are shown in fig. 2b-d. The scanned distance was 1 mm, with a step size of 10 µm. Each scan consists of 101 spectra.

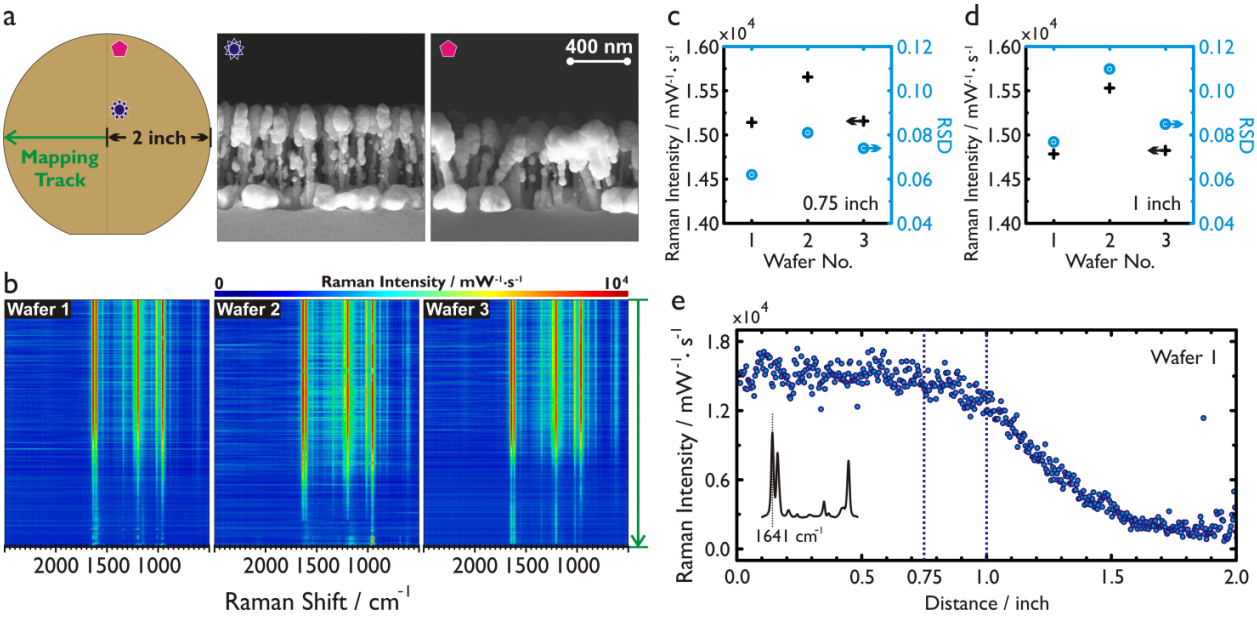

Fig. 5 (a) Schematic of the track for the SERS line scans in (b), plus cross-sectional SEM images of the fabricated Si NPs (~48 NPs μm^{-2}) near the middle and near the edge of a wafer. (b) Line scanned SERS spectra on three wafers following the track shown in (a). Each line scan started from the center of the 4-inch wafer towards its edge, with a step size of 100 µm. A scan consists of 509 spectra. The analyte was 10^{-4} M BPE dissolved in ethanol. The incubation time was less than 5 seconds. Clusters of the NPs were formed when the analyte solution evaporated. (c) - (d) The averaged SERS intensities and the corresponding RSDs of the 1641 cm^{-1} BPE peak, calculated according to the SERS maps in (b) for three different wafers. The statistical range for (c) and (d) is 0 – 0.75 inch and 0 – 1 inch, respectively, from the center of the wafer. (e) Trajectory plot of the SERS intensities at the 1641 cm^{-1} BPE peak for wafer 1 across the SERS line scan shown in (b).

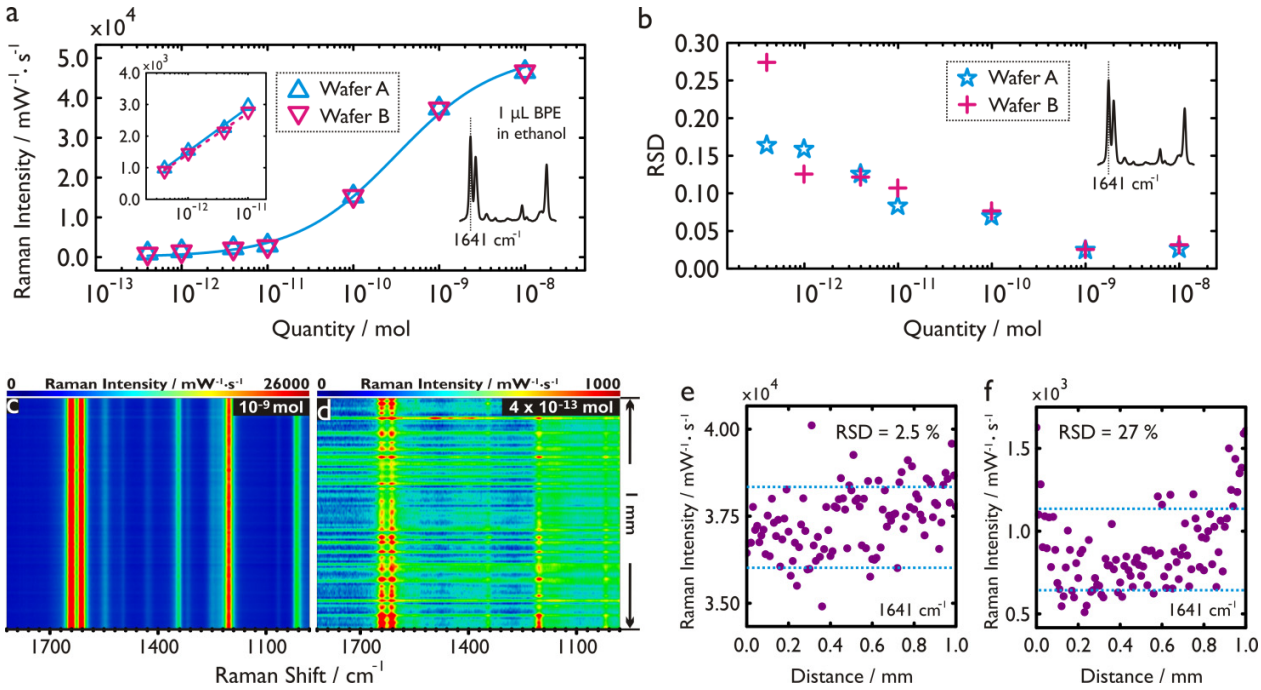

Fig. 6 SERS analyses of different quantity of BPE in 1 µL sample volumes of ethanol. The analyses were performed on two sets of specimens taken from two wafers. Only the specimens from the center of each wafer were used. Each specimen has ~1 x 1 cm^2 surface area. Clusters of NPs were formed by pipetting and drying of the analyte solution. A SERS line scan across 1 mm distance with a step size of 10 µm composed one analysis. (a) and (b) The recorded averaged SERS intensities and the corresponding RSDs at the 1641 cm^{-1} BPE peak. (c) and (d) Line-scanned SERS spectra on specimens taken from wafer B, at 10^{-9} mol and 4 x 10^{-13} mol, respectively. (e) and (f) The trajectory plots of the 1641 cm^{-1} BPE peak intensity corresponding to (c) and (d), respectively.

ASSOCIATED CONTENT

Supporting Information: Systematic optimization of the high-density NPs (~48 NPs μm^{-2}) in terms of SERS intensity, by changing the mask-less etching time and the deposition thickness of Ag; Dark-field scattering spectra of the optimized high-density NPs before and after clustering of the NPs; Distribution of the measured SERS intensities at the 1641 cm^{-1} BPE peak obtained on optimized NPs; Estimation of the SERS EF for the optimized NPs.

AUTHOR INFORMATION

Corresponding Author

*kaiwu@nanotech.dtu.dk

Author Contributions

The manuscript was written through contributions of all authors. All authors have given approval to the final version of the manuscript.

ACKNOWLEDGMENT

This work was funded by the IDUN project, The Danish National Research Foundation, Project DNRF122 and Villum Fonden, Grant No. 9301; the HERMES project, the European Research Council, Grant No. 320535; the NAPLAS project, the Danish Council for Independent Research.

REFERENCES

[1] P. L. Stiles, J. A. Dieringer, N. C. Shah, R. P. Van Duyne, *Annu. Rev. Anal. Chem.* **2008**; 1, 601.

[2] B. Sharma, R. R. Frontiera, A.-I. Henry, E. Ringe, R. P. Van Duyne, *Mater. Today* **2012**; 15, 16.

[3] C. Costas, V. López-Puente, G. Bodelón, C. González-Bello, J. Pérez-Juste, I. Pastoriza-Santos, L. M. Liz-Marzán, *ACS Nano* **2015**; 9, 5567.

[4] A. Barhoumi, N. J. Halas, *J. Am. Chem. Soc*. **2010**; 132, 12792.

[5] M. Käll, H. Xu, P. Johansson, *J. Raman Spectrosc*. **2005**; 36, 510.

[6] K. Kneipp, *Physics Today* **2007**; 60, 40.

[7] L. Tong, H. Xu, M. Käll, *MRS Bulletin* **2014**; 39, 163.

[8] E. C. Le Ru, P. G. Etchegoin, *Annu. Rev. Phys. Chem*. **2012**; 63, 65.

[9] S. Schlücker, *Angew. Chem. Int. Ed*. **2014**; 53, 4756.

[10] J. F. Li, Y. F. Huang, Y. Ding, Z. L. Yang, S. B. Li, X. S. Zhou, F. R. Fan, W. Zhang, Z. Y. Zhou, D. Y. Wu, B. Ren, Z. L. Wang, Z. Q. Tian, *Nature* **2010**; 464, 392.

[11] A. K. Samal, L. Polavarapu, S. Rodal-Cedeira, L. M. Liz-Marzán, J. Pérez-Juste, I. Pastoriza-Santos, *Langmuir* **2013**; 29, 15076.

[12] V, López-Puente, S. Abalde-Cela, P. C. Angelomé, R. A. Alvarez-Puebla, L. M. Liz-Marzán, *J. Phys. Chem. Lett*. **2013**; 4, 2715.

[13] L. Pérez-Mayen, J. Oliva, A. Torres-Castro, E. De la Rosa, *Nanoscale* **2015**; 7, 10249.

[14] D.-K. Lim, K.-S. J, J.-H. Hwang, H. Kim, S. Kwon, Y. D. Suh, J.-M. Nam, *Nat. Nanotechnol*. **2011**; 6, 452.

[15] W. Shen, X. Lin, C. Jiang, C. Li, H. Lin, J. Huang, S. Wang, G. Liu, X. Yan, Q. Zhong, B. Ren, *Angew. Chem*. **2015**; 127, 7416.

[16] H.-Y. Chen, M.-H. Lin, C.-Y. Wang, Y.-M. Chang, S. Gwo, *J. Am. Chem. Soc*. **2015**; 137, 13698.

[17] B. Sharma, M. F. Cardinal, S. L. Kleinman, N. G. Greeneltch, R. R. Frontiera, M. G. Blaber, G. C. Schatz, R. P. Van Duyne, *MRS Bulletin* **2013**; 38, 615.

[18] T. Li, K, Wu, T. Rindzevicius, Z. Wang, L. Schulte, M. S. Schmidt, A. Boisen, S. Ndoni, *ACS Appl. Mater. Interfaces* **2016**; 8, 15668.

[19] C. Hou, G. Meng, Q. Huang, C. Zhu, Z. Huang, B. Chena, K. Suna, *Chem. Commun*. **2014**; 50, 569.

[20] Y. Zhao, Y.-L. Zhang, J.-A. Huang, Z. Zhang, X. Chen, W. Zhang, *J. Mater. Chem. A* **2015**; 3, 6408.

[21] J. Li, C. Chen, H. Jans, X. Xu, N. Verellen, I. Vos, Y. Okumura, V. V. Moshchalkov, L. Lagaea, P. V. Dorpe, *Nanoscale* **2014**; 6, 12391.

[22] V. Merk, J. Kneipp, K. Leosson, *Adv. Optical Mater*. **2013**; 1, 313.

[23] X. Liu, Y. Shao, Y. Tang, K.-F. Yao, *Sci. Rep*. **2014**; 4, 5835.

[24] M. Hu, F. S. Ou, W. Wu, I. Naumov, X. Li, A. M. Bratkovsky, R. S. Williams, Z. Li, *J. Am. Chem. Soc*. **2010**; 132, 12820.

[25] A. Hakonen, M. Svedendahl, R. Ogier, Z.-J. Yang, K. Lodewijks, R. Verre, T. Shegai, P. O. Anderssonb, M. Käll, *Nanoscale* **2015**; 7, 9405.

[26] M. Yilmaz, M. Ozdemir, H. Erdogan, U. Tamer, U. Sen, A. Facchetti, H. Usta, G. Demirel, *Adv. Funct. Mater*. **2015**; 25, 5669.

[27] A. S. D. S. Indrasekara, S. Meyers, S. Shubeita, L. C. Feldman, T. Gustafsson, L. Fabris, *Nanoscale* **2014**; 6, 8891.

[28] Y. Lu, G. L. Liu, J. Kim, Y. X. Mejia, L. P. Lee, *Nano Lett*. **2005**; 5, 119.

[29] Q. Zhang, Y. H. Lee, I. Y. Phang, C. K. Lee, X. Y. Ling, *Small* **2014**; 10, 2703.

[30] H. Liu, X. Zhang, T. Zhai, T. Sander, L. Chen, P. J. Klarb, *Nanoscale* **2014**; 6, 5099.

[31] A. N. Severyukhina, B. V. Parakhonskiy, E. S. Prikhozhdenko, D. A. Gorin, G. B. Sukhorukov, H. Möhwald, A. M. Yashchenok, *ACS Appl. Mater. Interfaces* **2015**; 7, 15466.

[32] B.-B. Xu, Y.-L. Zhang, W.-Y. Zhang, X.-Q. Liu, J.-N. Wang, X.-L. Zhang, D.-D. Zhang, H.-B. Jiang, R. Zhang, H.-B. Sun, *Adv. Optical Mater*. **2013**; 1, 56.

[33] N. G. Greeneltch, M. G. Blaber, A.-I. Henry, G. C. Schatz, R. P. Van Duyne, *Anal. Chem*. **2013**; 85, 2297.

[34] N. G. Greeneltch, M. G. Blaber, G. C. Schatz, R. P. Van Duyne, *J. Phys. Chem. C* **2013**; 117, 2554.

[35] M. S. Schmidt, J. Hübner, A. Boisen, *Adv. Mater*. **2012**; 24, OP11.

[36] J. Yang, M. Palla, F. G. Bosco, T. Rindzevicius, T. S. Alstrøm, M. S. Schmidt, A. Boisen, J. Ju, Q. Lin, *ACS Nano* **2013**; 7, 5350.

[37] K. Wu, T. Rindzevicius, M. S. Schmidt, K. B. Mogensen, A. Hakonen, A. Boisen, *J. Phys. Chem. C* **2015**; 119, 2053.

[38] A. Hakonen, T. Rindzevicius, M. S. Schmidt, P. O. Andersson, L. Juhlin, M. Svedendahl, A. Boisen, M. Käll, *Nanoscale* **2016**; 8, 1305.

[39] H. Xu, E. J. Bjerneld, M. Käll, L. Börjesson, *Phys. Rev. Lett*. **1999**; 83, 4357.

[40] K. Wu, T. Rindzevicius, M. S. Schmidt, K. B. Mogensen, S. Xiao, A. Boisen, *Opt. Express* **2015**; 23, 12965.

[41] L. Morelli, K. Zór, C. B. Jendresen, T. Rindzevicius, M. S. Schmidt, A. T. Nielsen, A. Boisen, *Anal. Chem*. **2017**; 89, 3981.

[42] J. J. Castillo, T. Rindzevicius, K. Wu, M. S. Schmidt, K. A. Janik, A. Boisen, W. Svendsen, N. Rozlosnik, J. Castillo-León, *J. Nanopart. Res*. **2014**; 16, 2525.

[43] J. J. Castillo, T. Rindzevicius, K. Wu, C. E. Rozo, M. S. Schmidt, A. Boisen, *J. Raman Spectrosc*. **2015**; 46, 1087.

[44] M. Palla, F. G. Bosco, J. Yang, T. Rindzevicius, T. S. Alstrom, M. S. Schmidt, Q. Lin, J. Ju, A. Boisen, *RSC Adv*. **2015**; 5, 85845.

[45] R. K. Lauridsen, L. M. Sommer, H. K. Johansen, T. Rindzevicius, S. Molin, L. Jelsbak, S. B. Engelsen, A. Boisen, *Sci. Rep*. **2017**; 7, 45264.

[46] J. D. Caldwell, O. Glembocki, F. J. Bezares, N. D. Bassim, R. W. Rendell, M. Feygelson, M. Ukaegbu, R. Kasica, L. Shirey, C. Hosten, *ACS Nano* **2011**; 5, 4046.

[47] Y. S. Hu, J. Jeon, T. J. Seok, S. Lee, J. H. Hafner, R. A. Drezek, H. Choo, *ACS Nano* **2010**; 4, 5721.

[48] R. A. Gottscho, C. W. Jurgensen, D. J. Vitkavage, *J. Vac. Sci. Technol. B* **1992**; 10, 2133.

[49] A. Hakonen, P. O. Andersson, M. S. Schmidt, T. Rindzevicius, M. Käll, *Anal. Chim. Acta* **2015**; 893, 1.

[50] U. S. Dinish, C. Y. Fu, K. S. Soh, R. Bhuvaneswari, A. Kumar, M. Olivo, *Biosens. Bioelectron*. **2012**; 33, 293.